International Journal of Science and Research (IJSR)
ISSN: 2319-7064
SJIF (2022): 7.942

Feasibility of Estimating Type and Abundance of Iron Ore Using Field Hyperspectral Radiometry and Spectral Transformation in Precambrian Banded Iron Formations of North Odisha, India

Wasim Akram[1], Dibyendu Dutta[2], Jatisankar Bandyopadhyay[3]

[1, 3]Vidyasagar University, Midnapore, West Bengal, India

[2]Former RRSC/NRSC (ISRO), Kolkata, West Bengal, India
Corresponding Author Email: *ddisro[at]gmail.com*

Abstract: ***In large-scale mining operations, methods need to be developed for rapid estimation of the relative abundance of iron without prior knowledge of the distribution of rock types. Imaging spectroscopy is a promising tool to identify the type of iron alteration mineral and its total abundance. In the present study, ore samples from nine Odisha mines were examined for spectral variability, feature characterization, and derivative analysis with the objective of finding the best predictor variable for total iron content in routine mine operation. Band depth maxima was found to be the best predictive variable by virtue of a strong correlation (R^2 = 898) with total iron content, the lowest RMSE (5.61), and the highest ME (0.899). Further, to identify the spectrally dominant mineral in the assemblage, spectral matching was performed using spectral angular mapper (SAM), spectral correlation angle (SCA), and spectral information divergence (SID). The overall accuracy of mineral identification is highest for SCA, but SAM was found to be the best matching algorithm for hematite.***

Keywords: iron ore, imaging spectroscopy, spectral absorption feature, spectral matching algorithm

1. Introduction

Iron is a ubiquitous metal present on the Earth's surface in different forms based upon the alteration process, such as magnetite (Fe_3O_4), hematite (Fe_2O_3), goethite [FeO(OH)], limonite [$FeO(OH).nH_2O$], or siderite ($FeCO_3$). Due to weathering, ferrous iron is oxidized into insoluble ferric iron and transformed into hematite, goethite, and jarosite, commonly known as alteration minerals. Due to trans-opaque behavior, the ferric minerals exhibit color and spectral dominance even when present in small amounts in the mineral mixture [1]. The visible near infrared (VNIR) and short-wave infrared (SWIR) ranges, especially 650–1000 nm, are best used for mapping iron oxide minerals such as hematite and goethite [2]. Due to the unique crystal field transitions of iron-bearing minerals in the visible and near-infrared regions, especially at about 465 nm, 650 nm, and 850–950 nm [1, 3] of the spectrum, several attempts have been made by the researchers to quantify the absorption intensity as a proximal indicator of the abundance of iron by using various spectral transformation methods, including discrete bands, ratio indices, derivative analysis, and characterization of spectral absorption features by utilizing either the selective portion of the spectra or the whole spectra. The aim is to minimize the effect of variations in illumination geometry and background slope caused mostly by grain size [4]. However, the position of band depth maximum, depth, feature width, and shape are controlled by chemical structure, iron replacement by aluminum, and particle size [5, 6].

According to the Indian Bureau of Mines (2020), India is bestowed with a large deposit of iron ore, with an estimated reserve of 28.52 billion tons, of which 17.99 billion tons are hematite. Among different states, Odisha accounts for 57% of countries iron ore production, mostly in the form of hematite confined in the banded iron formation (BIF) of the Precambrian age. Hematite has high importance due to its high grade, which is conveniently used in the iron and steel industries. Presently, about 58 working mines are there, with a total area of more than 209 sq km, of which 153 sq km have been explored so far. Conventionally, grade estimation is done through wet geochemical analyses, which are not only time-consuming but costly, labor-intensive, and require expert personnel. But in large-scale mining operations, methods need to be developed for rapid estimation of the relative abundance of iron without prior knowledge of the distribution of rock types [4]. As the best alternative imaging technique, spectroscopy is capable of providing detailed spectral information in the shortest possible time, which can be effectively used for deriving the abundance or total iron content. A large number of studies have been carried out on mineral alteration, especially hydroxyl-bearing minerals, and lithology using space-borne multi-spectral and hyperspectral remote sensing [7–19]. However, broad multi-spectral bands cannot recognize the narrow, sensitive spectral bands of iron minerals for quantification of grade. In contrast, hyperspectral data with more than 100 narrow and contiguous spectral bands between 400 and 2500 nm is ideal for sensing the type of iron minerals and iron percentage in a rapid manner without destructive sampling and costly wet chemical analyses for economic grading. Keeping in view the ever-increasing demand for iron and steel and the gradual depletion of natural reserves, there is an emerging need to explore newer areas of potential zones with acceptable quality so that the extraction becomes economic. Hence, the broad objectives of the present research are: i) study of spectral variability or iron ores of different mines in north Odisha ii) chemometric analysis and predictive modeling, and iii) the ability of different spectral

matching techniques for identification of different ore types towards the feasibility of estimation of iron grades routinely in a rapid manner.

2. Study Area and Geological Setup

The study area is mostly confined to south-east of Sundargarh and the north-west of Keonjhar district, located between 21°44′09″N to 22°10′26″N latitude and 85°07′02″E to 85°28′06″E longitude. It consists of nine iron mines including Belkundi, Koida Bhadrashai 1&2, Sharda, Siljae, Dubune, Kadakale, Essel and Kurmitar (figure 1, annexure1). The region has a tropical to sub-tropical climate with a mean maximum temperature of 38-46°C (April-June) and total annual rainfall of 1535 mm. The physiography consists of moderately high hills, isolated hillocks, undulating plains and alluvial tracts. The region is mostly drained by Baitarani River, which flows along the north-south direction along the eastern half of the Keonjhar district. Forest and agricultural land cover 37.3% and 35.8% respectively.

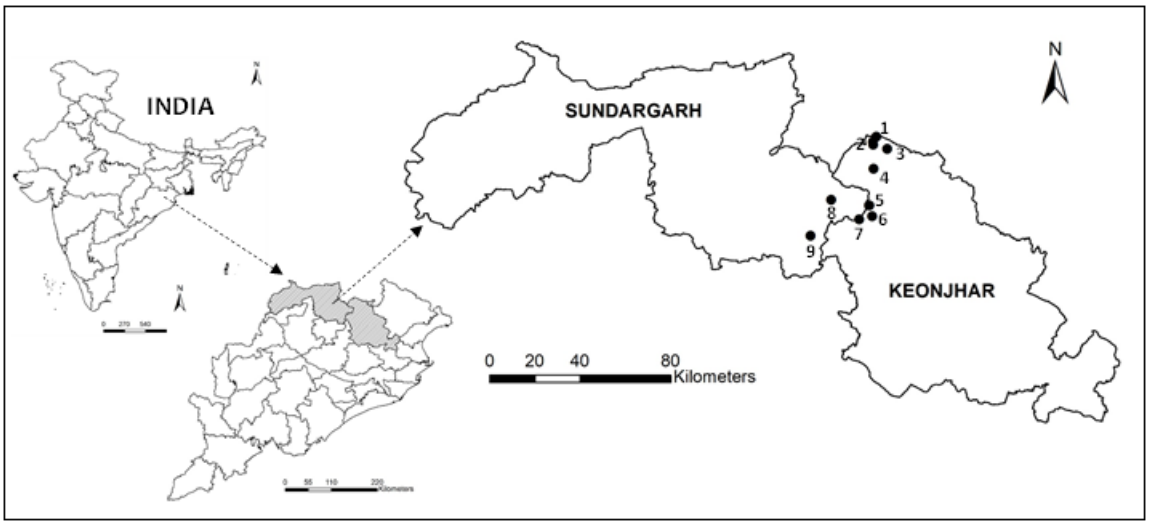

Figure 1: Location map of the study area [1) Belkundi, 2) Koida Bhadrashai 1, 3) Sharda, 4) Koida Bhadrashai 2, 5) Siljae, 6) Dubune, 7) Kadakale, 8) Essel, 9) Kurmitar]

The Keonjhar district is divided into 8 geological units, viz., i) patchy metamorphites belonging to the Archean age; ii) Singhbhum granite. iii) metasediments belonging to the Gorumahisani group of the Archean age; iv) volcano-sedimentary sequence intruded by Bonai granite belonging to the Archean and Paleoproterozoic; v) intrusives like chromiferous ultramafics, gabbro-anorthosite, dolerite, and quartz veins vi) sedimentaries and metasedimentaries belonging to the lower to middle Proterozoic; vii) laterites of the Cenozoic age; and viii) quaternaries represented by the Kaimundi Formation. The oldest of these groups, the Gorumahisani group of iron ore-bearing rocks, occurs around the northern, eastern, and southern borders of the granite body and consists of sheared pebbly quartzite, hornblende schist, and BHQ. The uppermost formation consists of hematite shale and phyllite, which are tuffaceous, and the base is made up of epidorite and hornblende schist. These rocks are tightly folded into a series of antiforms and synforms against the Singhbhum granite body, with axial planes dipping steeply away from it [20]. The Dhanjori group of metavolcanic rocks and tholeiitic lava flows (Dhanjori lava) occurs unconformably over the Gorumahisani group in the north-eastern and eastern parts of the platform and directly over the Singhbhum granite in the western part. This rock group is made up of a basal layer of quartzitic conglomerate overlain by cherty quartzite, chloritic and carbonaceous tuff, and phyllite. It is interlayered with tholeiitic lava flows and interbedded tuff and is barren of any iron or manganese ore. The Dhanjori group of rocks in the western part of the platform are deformed into a series of antiforms and synforms with axes plunging toward the northeast. The Noamundi group of iron and manganese ore-bearing rocks occurs with a slight break over the Dhanjori group in the western part of the platform in the Noamundi basin. This group is made up of shale-phyllite and tuff in the lower formation and shale, chert, and tuff in the upper formation, between which is a thick banded hematite jasper (BHJ) formation of thickness between 300 and 400 m and width up to 1000 m in some places. This extensive banded iron formation is much thicker than that of the Gorumahisani group. Massive hematite ore bodies of various sizes occur at or near the upper surface of the BHJ formation. The upper shale formation occurs in the core of the Noamundi basin and consists of considerable cherty and tuffaceous matter and interlayered beds of altered lava [21]. Made up of hematite, it is characterized by alternating bands or laminations with jasper in a parallel fashion. The Kolhan group of metapelitic rocks occurs with a marked unconformity over the Noamundi group and constitutes the small Kolhan basin in the north-western part of the platform. This group is made up of conglomerate at the base and sandstone shale and limestone at the top. The conglomerate contains BHJ pebbles in a sandy matrix that grades upward into current-bedded sandstone. The Kolhan group of rocks is almost flat to low-dipping in the eastern part of the Kolhan basin but is rather acutely folded as well as faulted in the western part of the basin. All four rock groups, viz., Gorumahisani, Dhanjori, Noamundi, and Kolhan, together are called the Iron Ore Supergroup (IOSG) in view of the occurrence of important banded iron formations. The major iron ore deposits of the Iron Ore Group are: i) Kudada-Patka-Groumahisani-Badampahar in the east (belt 1); ii) Tomka-Daiteri and Malayagiri-Sundarmundi in the south and southeast (belt 2); and iii) Jamda-Koira in the west (belt 3). Besides, there are two isolated occurrences: one

is at the Deo Nala section, and the other forms the Gandhamardan hill near Keonjhar [22].

3. Materials and Methodology

3.1 Field Hyperspectral Data Collection and Preprocessing

The field spectra were obtained using an HR-1024 spectro-radiometer vertically above the rock surface using a 14° field-of-view lens during local solar noon (i.e., between 12:00 and 13:00 IST) when the solar zenith is minimal and atmospheric humidity reaches a minimum. The instrument was positioned by pointing downward to measure the upwelling radiance in the 350–2500 nm wavelength region. The instrument was configured to take 20 simultaneous readings for integration and store them as single data points. The radiance received from the object is calibrated into reflectance using the Spectralon reflectance panel. The dark current, or electronic noise that is generated in the absence of any light entering the optics is automatically corrected. The instrument records spectral reflectance between 350 and 2500 nm with a sampling interval of 1.4 nm (FWHM of 3 nm) for 350–1000 nm and 2 nm (FWHM of 10 nm) for the 1000–2500 nm spectral region.

Various pre-processing performed includes noise suppression and data smoothing using Savitzky-Golay [23] least squares polynomial regression, which is calculated around each point, a new smooth value is created, and the shape is retained as the original signal. A third-order polynomial with a window size of 10 was used in the study. Next, data scaling at a 1 nm spectral interval was done for the spectral matching requirement between target and reference library spectra, as both are of different ranges and spectral resolutions. De-convolution was carried out to separate the spectrally overlapped features by using the modified Gaussian model [24]. Mathematically, the MGM is given as follows:

$$g(x) = s.\exp\left[\frac{-(x-\mu)^2}{2\sigma^2}\right] \quad \text{.....(i)}$$

where x = wavenumber, s = amplitude of the distribution, μ = centre (mean) wavenumber, and σ = the width.

3.2 Collection of Reference Spectral Library Data

The reference library spectra of iron-bearing rocks and minerals, along with other mineral assemblages, were obtained from the USGS, JPL, and JHU data repositories. The spectral data is available in ASCII format, along with ancillary information. The ancillary data file contains sample description, mineral name, class, subclass, particle size, origin, XRD analysis, and percentages of SiO_2, Al_2O_3, FeO, MgO, CaO, K_2O, Na_2O, TiO_2, and MnO. The ASCII data was converted to spreadsheet format. Like field spectra, the library spectra was also rescaled. The rescaled library spectra were further smoothed using the procedure given by Savitzky-Golay [23]. A total of 70 library spectra were collected, including goethite, hematite, magnetite, pyrite, and siderite minerals.

3.3 Absorption Feature Recovery and Attribution

Prior to absorption feature characterization, the continuum was removed within the region of the spectral absorption feature by defining a spectral continuum for each spectrum and then dividing the spectrum by the continuum. This process normalized the variations in brightness [3] and placed all the absorption features on a common reference plane in order to allow comparison of individual absorption features from a common baseline [25]. The continuum-removed spectra were characterized for maximum band depth relative to the continuum, area under the curve [26], full width at half maxima, and skewness. The band depth (BD) at each wavelength in the absorption feature is calculated by subtracting the continuum removed reflectance (CRR) from '1' as was given by Kokaly & Clark [27].

Band depth (BD_λ) = 1- CRR_λ .....(ii)

Where $CRR_\lambda = R/R_c$

Area under the absorption curve =

$$\int_{\lambda_{end}}^{\lambda_{start}} BD \quad \text{.....(iii)}$$

Where

CRR_λ = continuum removed spectra

BD_λ = band depth at a given wavelength

BD_{max} = band depth maxima

λ_{start} , λ_{end} = The wavelength of the start point and end point in an absorption curve

Skewness is a measure of the asymmetry of the probability distribution of a real-valued random variable about its mean and can be quantified to define the extent to which a distribution differs from a normal distribution. Mathematically, it is defined as the sum of reflectance over the number of channels to the right of the band depth maxima divided by the sum of reflectance over the number of channels to the left of the band depth maxima. Full Width at Half Maximum (FWHM) is the width of a spectrum curve measured between those points on the y-axis that are half the maximum amplitude.

3.4 Spectral Matching

The spectral matching aims to find spectral similarity between a reference library and target spectra in terms of spectral distance. Generally, the unknown spectra (target) are compared against the reference spectral library data by using a distance metric produced by different search algorithms. Two spectra are considered to be similar when the overall spectral distance between them is small (less than the threshold) and dissimilar otherwise. A list of target reference spectra is generated by the search algorithms based upon the numerical similarity score. '*Most similar*' library spectra top the hit-list. Deterministic algorithms exploit the geometrical and physical aspects of unknown and reference spectra. They are mathematically simple and easier to implement. In contrast, stochastic algorithms evaluate the statistical distribution of spectral reflectance values of target endmembers. They are more accurate but mathematically complex and require huge computing resources. In the present study two deterministic algorithms [Spectral Angle Mapper (SAM), Spectral Correlation Mapper (SCM)] and one

stochastic algorithm [Spectral Information Divergence (SID)] were used to harness the best of each algorithm. The mathematical formulations of the algorithms are given below.

3.4.1 Spectral Angle Mapper (SAM)

SAM was proposed by Yuhas and Goetz [28], which is a physically-based spectral classification in which the spectral angle between the unknown and reference spectrum is calculated. Smaller angles represent closer matches to the reference spectrum. This method is insensitive to illumination and albedo effects since the algorithm uses only the vector direction and not the vector length. The spectral variation between two spectra, Si and Sj, computed over wavelength λ, can be quantified by the spectral angle between the vectors as follows:

$$SAM(s_i, s_j) = cos^{-1}\left(\frac{\sum_{l=1}^{L} s_{il} s_{jl}}{\left[\sum_{l=1}^{L} s_{il}^2\right]^{1/2}\left[\sum_{l=1}^{L} s_{jl}^2\right]^{1/2}}\right) \quad \text{.....(iv)}$$

3.4.2 Spectral Correlation Mapper (SCM)

The SCM [29, 30] is a derivative of the Pearson correlation coefficient, which calculates the cross-correlation coefficient between an unknown spectrum and a reference spectrum at different match positions by shifting the reference spectrum over spectral channels relative to the unknown spectrum [29]. The coefficient is a dimensional index, the value of which varies between -1 and 1 and reflects the extent of the linear relationship between the two spectra. The SCM between two spectra, Si and Sj, is given by:

$$SCM_{(s_i,s_j)} = \frac{n\sum_1^n s_i s_j - \sum_1^n s_i \sum_1^n s_j}{\sqrt{\left[n\sum_1^n s_i^2 - (\sum_1^n s_i)^2\right]\left[n\sum_1^n s_j^2 - \left(\sum_1^n s_j\right)^2\right]}} \quad \text{.....(v)}$$

$$SCA(S_i, S_j) = Cos^{-1}\left(\frac{r_{si,sj}+1}{2}\right) in\ radians \quad \text{.....(vi)}$$

Where *'n'* is the number of overlapping spectral bands. To compare with other measures the coefficient converted in to an angle through a formula:

3.4.3 Spectral Information Divergence (SID)

SID [31] is based on the concept of divergence in information theory and can be used to describe the statistics of a spectrum. The SID views each unknown or target spectrum as a random variable and then measures the discrepancy of probabilistic behaviors between two spectra. Spectral similarity is calculated based on the distance between two vectors in terms of their corresponding probability mass functions.

3.5 Spectral Derivatives

For derivative analysis, the first Svitzky-Golay smoothing filter [23] was applied to reduce the noise, and then the derivative analysis was performed. The amplitude of derivatives changes with the width of the smoothing window, and hence a smoothing filter of 60 bands was used so that the noise is suppressed and the ferric absorption features are preserved [4]. In the present study, both the 1st and 2nd derivatives were calculated, but only the 2nd derivative was used as the relationship with the 1st derivative and the percentage weight of iron minerals were reported to be poor [4]. Due to very high noise, the 4th derivative was also not used in the present study.

Mathematically, if $y = f(x)$, then $dy/dx = f'(x)$; now if $f'(x)$ is differentiable, then differencing dy/dx, again with respect to x we get 2nd order derivative i.e.

$$\frac{d}{dx}\left(\frac{dy}{dx}\right) = \frac{d^2y}{dx^2} = \boldsymbol{f''(x)} \quad \text{.....(vii)}$$

3.4.4 Laboratory Chemical Analyses

The field-collected samples were subjected to detailed analysis of the weight percentages of Fe, Mn, SiO_2, Al_2O_3, and MgO content. Standard analytical procedures were used following the method given in the manual of the Indian Bureau of Mines [32]. Fe was estimated using dichromate, MgO by EDTA complexometry, Al_2O_3 by EDTA complexometry and back titration, Mn by periodate oxidation followed by spectrophotometry, and SiO_2 by the gravimetric method.

3.4.5 Model Validation

The modelled iron weight percentages were compared against observed chemical analysis results using the coefficient of determination (R^2), root mean square error (RMSE), coefficient of residual mass (CRM), a -ve value indicating that the majority of modelled values are greater than the observed values, and a +ve value indicating vice versa [33], and modeling efficiency (ME) to evaluate the errors in the modelled Fe%. The formulae for RMSE, CRM, and ME are given below.

$$RMSE = \sqrt{\frac{1}{n}\sum_{i=1}^{n}(P_i - O_i)^2} \quad \text{.....(viii)}$$

$$CRM = \frac{\sum_{i=1}^{n} O_i - \sum_{i=1}^{n} P_i}{\sum_{i=1}^{n} O_i} \quad \text{.....(ix)}$$

$$ME = 1 - \frac{\sum_{i=1}^{n}(P_i - O_i)^2}{\sum_{i=1}^{n}(P_i - \bar{O})^2} \quad \text{.....(x)}$$

Where P_i = modelled value, O_i = observed value, $\bar{O}$ = observed mean, n = number of observations. The ME is sensitive to extreme values and might yield sub-optimal results when the dataset contains large outliers. For perfect match, the ME value is one. The ME value close to 1 indicates more accurate model.

4. Results and Discussion

4.1 Spectral Variability of the Iron Ore Samples

Spectral curve of the iron ores are characterized by intense ligand-to-metal charge-transfer band in the ultra-violet region (< 400 nm), which caused sharp drop off in intensity at the shortwave end of visible spectrum. The uptrend is apparent from 500 nm, and peak value occurs between 750 and 800 nm since the reflectance is more in the red region due to the trans-opaque behaviour of ferric iron. Thereafter, the reflectance decreases, forming a well-defined wide absorption feature in the visible near-infrared region between 700 and 1250 nm with absorption maxima between 880 and 1000 nm due to Laporte-forbidden transitions [34, 35]. The presence of a weak band near 640 nm and intense band ~900 nm can readily be assigned to the ferric iron transition $^6A_{1g} \rightarrow {}^4T_{2g}$ and $^6A_{1g} \rightarrow$

$^4T_{1g}$ and ligand field transitions of Fe^{3+}, respectively. Ferric minerals most commonly exhibit absorption bands near 900 nm due to spin-forbidden transitions in ferric iron [36, 34]. After 1250 nm, the spectral curves exhibit either monotonously increasing reflectance or droop down towards longer wavelengths with sharp absorption features of different intensity between 1420-1450 nm, 1920-1945 nm, and 2200-2280 nm due to vibrational overtone or combination tones of the fundamental modes of hydroxyl groups bound at different locations of the lattice. These absorption features are narrow, and the depth and width vary widely.

In hematite-dominated minerals intense absorption was observed in the visible to about 550 nm and a well-developed reflectance minima near 855 nm due to ferric iron $^6A_{1g} \rightarrow {}^4T_{1g}$ transition [37]. Hematite absorption between 848 and 887 nm was observed in ESSEL, SAIL, Joda east, Koida bhadrashai, Belkundi, Sarda Kadakale, and Siljae, which matches with the observations of Morris et al. and Vaughn & Tossell [34, 38], who reported the hematite absorption between 846 and 870 nm region. However, in goethite, the intense reflectance minima is less extensive than hematite and confined to 500 nm. Large variability exists in the magnitude of reflectance values among the samples of different iron mines. The range of minimum reflectance (R_{min}) is 1.82% (S-60) to as high as 8.63% (S-1). The range of magnitude of reflectance maxima (R_{max}) is much higher than reflectance minima, ranging from 6.67% in S-66 to 57.18% in S-49. The prominent absorption feature between 700 and 1250 nm was missing in some of the samples of Kurmitar, Belkundi, Kadakale and Siljae mines (S-71, S-72, S-77 and S-79). Some of the samples from Siljae, Joda, Belkundi and Sarda mines are shifted towards longer wavelengths (> 920 nm). This apparent shift could be due to aluminium substitution in hematite and goethite (the $^6A_{1g} \rightarrow {}^4T_{1g}$ transition) [39]. Aluminium substitution in hematite and goethite causes an apparent shift of the NIR reflectance minimum near 860 nm (the $^6A_{1g} \rightarrow {}^4T_{1g}$ transition) toward longer wavelengths. Besides chemical composition, particle size, porosity, crystallographic orientation and packing also affect the spectral features. Clark & Roush [3] have stated that larger grain sizes show increased saturation of the 900 nm absorption of iron, broadening and shifting the apparent reflectance minimum to longer wavelengths. Most of the mines spectra show very wide and deep iron absorption in the 700-1250 nm region, except some of the samples from Koida bhadrashai, Sarda, Kadakale and Siljae. Large variability in the location of the iron absorption feature was also noticed, wherein the starting (λ_{start}) and ending (λ_{end}) wavelength varies from 703-810 nm and 1030-1246 nm, respectively, which indicates the variability is almost double at the longer wavelength end of the feature in comparison to shorter wavelength side. Distinct goethite absorption between 896 and 932 nm [34] was observed in Joda east, Sarda, Rungta, Siljae and Siljoda-Kalimati (sample no S-4, 5, 7, 8, 40, 56, 58, 30, 49), mostly near 860 and 912 nm. The broad, well-developed reflectance minima occurring near 930 nm in Sarda and Siljae is due to ferric iron $^6A_{1g} \rightarrow {}^4T_{1g}$ transition in goethite. Two of the samples viz., Sarda (S-8) and Siljae (S-2), have absorption feature at 420 nm, which could be due to $^6A_{1g} \rightarrow {}^4T_{1g}$, ^4E_g transition, and a broad, well-developed feature near 930 nm due to the $^6A_{1g} \rightarrow {}^4T_{1g}$ ferric iron transition, which resembles to jarosite [37]. Mean spectral profiles of different iron ore samples collected from north Odisha mines are given in figure 2.

The spectral profiles of different alteration minerals and their assemblages are given in figure 3, where banded hematite quartzite (BHQ) and laterites show low reflectance in comparison to limonite and goethite and banded hematite jasper (BHJ). Laterization of BHJ have higher overall reflectance in comparison to laterites. The reflectance peak around 750 nm and the depth of the absorption maxima between 750 and1200 nm also vary significantly. The depth of the absorption feature between 750 and 1250 nm is very shallow and short in lateriate and BHJ/Q.

4.2 Absorption Features (700-1250 nm region) and Characterization

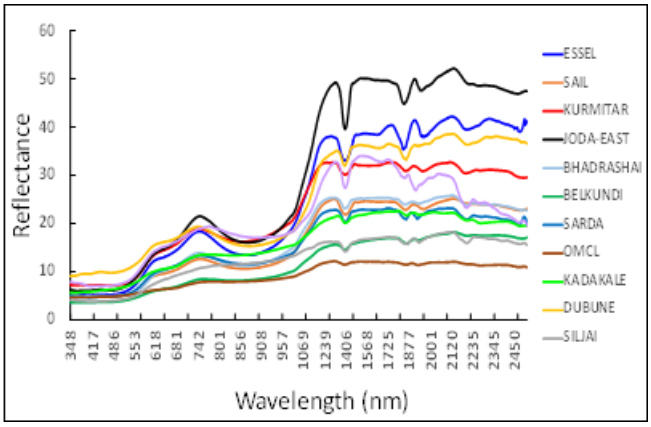

Figure 2: Mean spectral profile (348-2500 nm) of iron ores collected from different mines

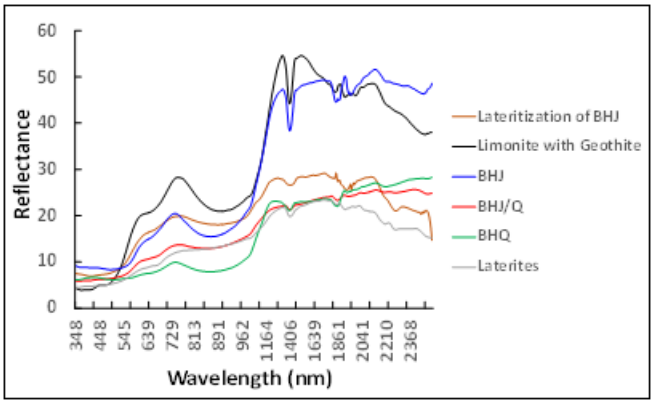

Figure 3: Reflectance spectra of different alteration products

The location, depth, width and shape of the ferric absorption features were further analysed for correlation with the total iron content (wt%) and to develop an empirical model. These features are controlled by crystal structure and, hence, can be related to the mineralogy of the sample [40]. Keeping in view the characteristics of iron-bearing rocks and minerals, the 700-1250 nm region was selected for continuum removal and further characterization of absorption features, viz., the wavelength of start and end of the feature (λ_{start}, λ_{end} respectively), maximum band depth (BD_{max}), wavelength position at maximum band depth (λBD_{max}), absorption curve area, full-width at half the maximum of the band depth (FWHM), and skewness. The summary statistics of the absorption features of the studied samples is given in Table 1.

Table 1: Summary statistics of the iron absorption feature (700-1250 nm)

Parameter	Min	Max	Mean	CV
λ_{start}	703.0	810.6	745.89	2.43
λ_{end}	1030.1	1246.5	1187.78	5.26
$\Delta\lambda$	36.2	370.7	233.45	27.25
BD_{max}	0.034	0.641	0.32	51.08
λBD_{max}	882.8	1007.0	907.78	2.81
Area	3.39	113.34	52.58	55.63
Skew	0.731	5.001	1.24	110.36

The variability of skewness, curve area and band depth maxima is very large. A higher band depth (> 0.5) was found in 10 samples including Essel, Joda east, SAIL, Kurmiar, Koia Bahdrasahi and Sarda mine. In contrast very low band depth (< 0.1) was obtained from the mine overburden samples of Kurmitar, Kadakale and Siljae. The intensity of the band depth is an indication of the amount of the absorbing minerals present in the rock samples. Almost 48% of the samples exhibited λBD_{max} between 800-900 nm but in S-11, S-19, S-27, S-30, S-51, S-52, S-65, S-70, S-74 and S-78, the location of band depth maxima is shifted towards longer wavelength. Careful examination of those samples reveal that the Al_2O_3 content is significantly high (13.95–29.95%) in those samples. According to Buckingham [39] aluminium substitution in hematite and goethite causes an apparent shift of the NIR reflectance minima ($^6A_{1g} \rightarrow {}^4T_{1g}$ transition) towards longer wavelengths. The wavelength of band depth maxima (λBD_{max}) varied based upon the mineral composition and metallic substitution in the crystal lattice. The area of absorption curve is as low as 3.39 in S-67 to 112.24 in S-37. Jarmer and Schutt [47] observed direct relationship between reflectance features and the iron content and noted that there is a close relationship between the area of the iron absorption feature and total iron content. Their study indicate that the area and position of absorption features can be used for characterizing the iron ores by extracting certain spectral parameters by hyperspectral radiometric studies. In the present study most of the samples are left skewed as the skewness values are less than 1.0; however, some of samples (S-30, S-55, S-60 and S-74) are highly right skewed (skew > 2.0).

4.3 Spectral Derivatives

Spectral derivatives have been used to quantify iron oxides [42, 4, 43-45]. The advantage of derivatives is that they can effectively remove the background slope effect of the spectra by minimizing the effect of illumination variation [46]. Several researchers pointed out that 2nd and 4th derivative gives significantly better results than the 1st derivative in quantifying the distribution of ferric iron minerals [4, 44, 45]. Due to presence of significant amount of noise in 4th derivative after smoothing, only 2nd derivative has been used for the present study. The 2nd derivative values were integrated over 430-970 nm region [4] to correlate the abundance of iron minerals (% weight). The 2nd derivative graph of some of the hematite and goethite samples are given in figure 4.

4.4 Chemometric Analysis

Chemometrics is the use of mathematical and statistical methods to improve the understanding of chemical information and to correlated quality parameters or physical properties to analytical data. This method can be used as a quality control tool for rapid authentication from a wide variety of ore samples. In the present study, an attempt has been made to develop the predictive models by using certain key spectral parameters to relate geochemical parameters of total iron content to the ores. The summary statistics of the percentage weight of different elements and oxides are given in Table 2. From Table 2, it can be seen that there is large variation in Fe content, which varies between 8.37 and 68.07% with low coefficient of variation. About 62% of the samples had %Fe greater than 50%. Five of the samples have very low Fe%, constituting less than 20% of the mine overburdens. The variability of Mn% was very high (CV = 293.12%). About 87% of the samples have Mn content less than 1%. Only four samples have higher Mn% ranges from 24.48% to 39.10%.

Table 2: Summary statistics of weight percentage of different elements and oxides

Parameter	Min	Max	Mean	CV (%)
Fe (%)	8.37	68.07	50.52	32.64
Mn (%)	0.025	39.1	2.69	293.12
SiO_2 (%)	0.57	55.76	10.56	127.50
Al_2O_3 (%)	0.35	31.55	6.91	108.70
MgO (%)	0.036	0.64	0.11	134.33

For the development of empirical models, the samples were divided into two groups, in which 45 samples were used for model development and 28 samples for model validation, keeping in view the representation of different mines and the wide range of total iron content. Some of the samples could not be utilized as they did not exhibit well-developed absorption maxima for ferric iron. From figure 5, it is apparent that the exponential relationship is better ($R^2 = 0.914$) than the linear relationship in both band depth maxima curve areas, as the sensitivity decreases with a higher total Fe% (> 60%). The empirical models developed were based on BD_{max}. The curve area and integrated 2nd derivative are given below.

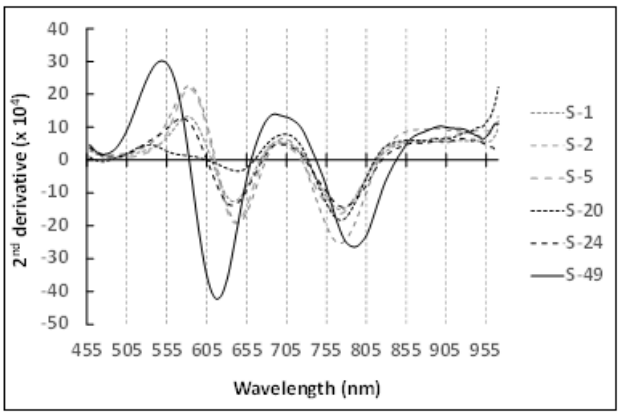

Figure 4: Second derivative spectra of some of the hematite (S-1M S-5, S-20) and goethite (S-2, S-24, S-49) samples

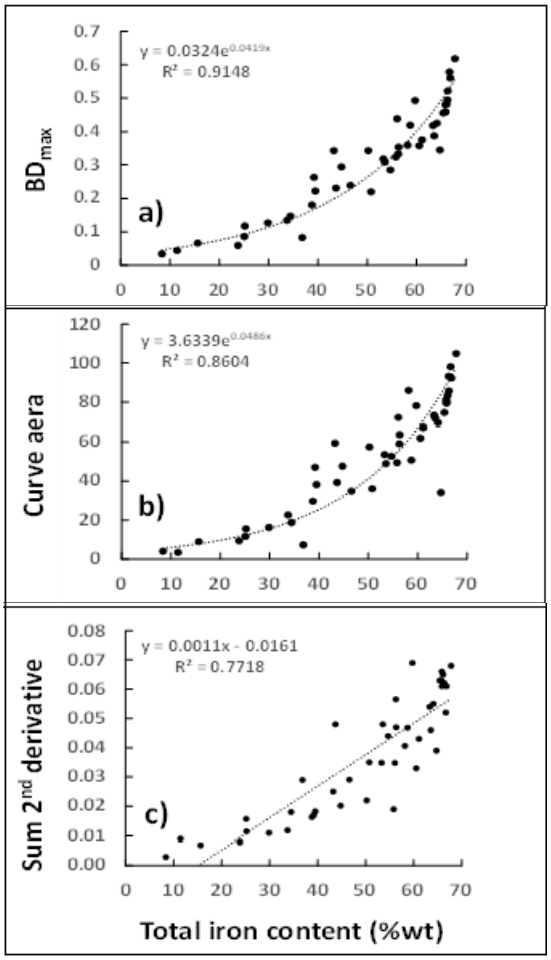

Figure 5: Scatterplot between total Fe% and a) BD_{max} b) curve area and c) sum of derivative between 430-970 nm

$y_1 = 0.0324 * e^{0.0419x}$, where y_1 = band depth maxima and x = total iron (weight%)
$y_2 = 3.6339 * e^{0.0486x}$, where y_2 = curve area and x = total iron (weight%)
$y_3 = 0.0011x – 0.0161$, where y_3 = sum of 2nd derivative and x = total iron (weight%)

In the next step models performance was examined to choose the best predictor variable for total iron content using coefficient of determination (R^2), RMSE, CRM and ME values given in Table 3. The correlation between modelled and measured iron content is significant in all the parameters, which indicates that the modelled values are in good agreement with the measured values. The correlation is strongest with BD_{max} among the three spectral parameters. The RMSE is 5.612% which is more than two times less than 2nd derivative. The high RMSE value of the 2nd derivative could be attributed to the increased uncertainties in the input parameters values. The ME values between 0.698 and 0.899 indicate the good performance of the model. The CRM indicates the overall under- or over-estimations. For a perfect estimation, the value should be close to zero. Both the BD_{max} and curve area exhibited values close to zero. The negative CRM value of 2nd derivative indicates that the majority of the modelled values are greater than the measured values.

Table 3: Error estimates between modelled and observed values

	BD_{max}	Curve area	2nd derivative (430-970 nm)
R^2	0.898*	0.790*	0.802*
RMSE	5.612	8.619	13.111
CRM	0.001	0.000	-0.154
ME	0.899	0.790	0.698

Values are significant at 0.001 level (df = 44)

4.4 Spectral Matching

For spectral matching preference, 70 iron minerals, viz., coarse and fine-grained hematite, hematite-coated quartz, nano-hematite, hematite thin film, magnetite, goethite, goethite-phyllite, limonite, pitch limonite, pyrite, and siderite, as well as a number of other silicate, hydroxyl, and oxide minerals, were used. All the library and target (field) spectra were scaled at a 1nm interval, and thereafter, the three most commonly used matching algorithms, viz., SAM, SCA, and SID, were utilized. Both SAM and SCA are deterministic, whereas SID is a stochastic algorithm. The spectral similarity is measured based on spectral angle and correlation in the case of deterministic types and divergence and probability for stochastic types. Out of 80 field samples, only 65 were selected, which consist of the three most prevalent alteration minerals in the region, viz., hematite, goethite, and hematite-coated quartz. The best matching algorithm was selected based on the threshold value (< 0.1). The overall accuracy and class accuracy are given in Table 4. Overall accuracy is highest (93.85%) for SCA and lowest (78.76%) for SID. The hematite was best predicted by SAM and the goethite by SCA.

Table 4: Prediction accuracy by different matching algorithms in percent

	Hematite	Goethite	Hematite coated quartz	Overall accuracy
SAM	100	75	86.15	86.15
SCA	88.89	100	93.85	93.85
SID	74.07	83.33	78.46	78.76

5. Conclusions

The present study was carried out to demonstrate the potential of hyperspectral radiometry to yield quantitative and qualitative information on the abundance of iron minerals and dominant ferric minerals. To achieve the goal, field hyperspectral data collected from nine iron ore mines in Odisha were analyzed for spectral absorption features, viz., band depth maxima and curve area, as well as the second derivatives integrated over the visible near-infrared region to find the best proximal indicator for quick appraisal and grading of the iron ores without going for detailed laboratory-based analysis. Most of the spectral curves exhibited an intense charge transfer band in the lower wavelength of the visible spectrum and a well-defined absorption feature in the 700–1250 nm region. The location of band depth maxima slightly shifted towards a longer wavelength based on aluminium substitution for ferric iron. Total iron content was strongly correlated with absorption features and the derivative integrals. A strong correlation between spectral features and iron oxide content would lead to the development of empirical models that would enable the estimation of the grade of iron ores in a rapid manner in mining operations. Based upon the correlation, RMSE, CRM, and ME band depth maxima were

found to be the best predictor variables for total iron content. Besides quantification, identification of spectrally dominant minerals was done using the three most commonly used matching algorithms, viz., SAM, SCA, and SID. Among the three algorithms, the overall accuracy was highest for SCA, but the best matches for hematite and goethite were SAM and SCA, respectively. This information is invaluable for automated grading in the mining process.

6. Future Scope

The present study was carried out based on limited samples from selected mines. Further work needs to be carried out to develop robust models of ferric iron content from different rock types. Besides, automation of spectral feature recovery and data-driven optimal feature identification in a machine learning environment need to be explored for faster and more operational grading of iron ore samples.

Acknowledgements

The authors thankfully acknowledge the field support and logistics extended by the scientists of the Odisha Remote Sensing Application Centre and the mine managers. The chemical analyses of the rock samples by the office of the Deputy Director (CA), Joda, Keonjhar, are duly acknowledged. Thanks are also due to Shri Prabhat Kanti Rout and Shri Sourav Samanta for accompanying them on the field visit. The study could not have been possible without the availability of library spectra of iron-bearing rocks and minerals from USGS, JPL, and JHU.

References

[1] T.E. Townsend, "Discrimination of iron alteration minerals in visible and near-infrared reflectance data". Journal of Geophysical Research: Solid Earth, 92(B2), pp. 1441-1454, 1987.
[2] S.K. Raj, S.A. Ahmed, S.K. Srivatsav, P.K. Gupta, 2015. "Iron Oxides Mapping from E0-1 Hyperion Data", Journal Geological Society of India, 86, pp. 717-725, 2015.
[3] R.N. Clark, T.L. Roush, Reflectance spectroscopy: Quantitative analysis techniques for remote sensing applications", Journal of Geophysical Research: Solid Earth, 89 (B7), pp. 6329-6340, 1984.
[4] R.J. Murphy, S.T. Monteiro, "Mapping the distribution of ferric iron minerals on a vertical mine face using derivative analysis of hyperspectral imagery (430-970 nm)", ISPRS Journal of Photgrammetry and Remote Sensing, 75, pp. 29-39, 2013.
[5] T. Cudahy, E.R. Ramanaidou, "Measurement of the hematite : goethite ratio using field visible and near-infrared reflectance spectrometry in channel iron deposits, Western Australia", Australian Journal of Earth Sciences, 44, pp. 411-420, 1997.
[6] E. Ramanaidou, M. Wells, D. Belton, M. Verrall, C. Ryan, "Mineralogical and Microchemical Methods for the Characterization of High-Grade Banded Iron Formation-Derived Iron Ore", In Banded Iron Formation-related High-grade Iron Ore, Society of Economic Geologists, S. Hagemann, C.A. Rosière, J. Gutzmer, N.J. Beukes (eds.), 15, pp. 129-156, 2008.
[7] M.J. Abrams, D. Brown, L. Lepley, R. Sadowski, "Remote sensing for porphyry copper deposits in southern Arizona", Economic Geology, 78(4), pp. 591-604, 1993.
[8] H. Kaufmann, "Mineral exploration along the Aqaba-Levant structure by use of TM-data: concepts, processing and results", Int. J. Remote Sens. 10, pp. 1639–1658, 1988.
[9] A.P. Crosta, J.M. Moore, "Geological mapping using Landsat thematic mapper imagery in Almeria Province, South-east Spain", International Journal of Remote Sensing, 10 (3), pp. 505-514, 1989.
[10] S.J. Fraser, "Discrimination and identification of ferric oxides using satellite Thematic Mapper data: A Newman case study", Int. J. Remote Sens., 12, pp. 635–641, 1991.
[11] L.C. Rowan, J.C. Mars, C.J. Simpson, "Lithologic mapping of the Mordor, NT, Australia ultramafic complex by using the Advanced Spaceborne Thermal Emission and Reflection Radiometer (ASTER)", Remote Sens. Environ. 99, pp. 105–126, 2005.
[12] Y. Ninomiya, B. Fu, T.J. Cudahy, "Detecting lithology with Advanced Spaceborne Thermal Emission and Reflection Radiometer (ASTER) multispectral thermal infrared radiance-at-sensor data", Remote Sens. Environ. 99, pp. 127-139, 2005.
[13] L. Liu, D.F. Zhuang, J. Zhou, D.S. Qiu, "Alteration mineral mapping using masking and Crosta technique for mineral exploration in mid-vegetated areas: A case study in Areletuobie, Xinjiang (China)", Int. J. Remote Sens. 32, pp. 1931–1944, 2011.
[14] F.A. Kruse, J.W. Boardman, J.F. Huntington, "Comparison of airborne hyperspectral data and EO-1 Hyperion for mineral mapping", IEEE Transactions on Geoscience and Remote Sensing, 41(6), pp. 1388–1400, 2003.
[15] P. Debba, F.J.A. Van Ruitenbeek, F.D. Van Der Meer, E.J.M. Carranza, A. Stein, "Optimal field sampling for targeting minerals using hyperspectral data", Remote Sensing of Environment, 99(4), pp. 373-386, 2005.
[16] E. Ramanaidou, P. Connor, A. Cornelius, S. Fraser, "Imaging spectroscopy for iron ore mine faces", in: Iron Ore Conference, Perth, WA, Australia, 9–11th September, pp. 155–157, 2002.
[17] R.J. Murphy, S.T. Monteiro, S. Schneider, "Evaluating classification techniques for mapping vertical geology using field-based hyperspectral sensors", IEEE trans. Geoscience and Remote Sensing, 50, pp. 3066–3080, 2012.
[18] T. Magendran, S. Shanmugam, A.K. Bhattacharya, "Hyperspectral radiometry to quantify the grades of iron ores of Noamundi and Joda mines, Eastern India", J. Indian Soc. Rem. Sens., 39(4), pp. 473-483, 2011.
[19] A. Sengupta, M.D. Adhikari, S. Maiti, S.K. Maiti, P. Mahanta, and S. Bhaumick, "Identification and mapping of high-potential iron ore alteration zone across Joda, Odisha using ASTER and EO-1 hyperion data", Journal of Spatial Science, 64(3), pp. 491-514, 2019.
[20] A.K. Banerji, "Structure and stratigraphy of part of northern Singhbhum, south of Tatanagar, Bihar", Proc. Nat. Inst. Sci, India, 30A, pp. 486-510, 1964.
[21] J.A. Dunn, "Stratigraphy of south Singhbhum", Memoir, Geological Survey of India, 63, pp. 303-369, 1940.

[22] H.N. Bhattacharya, I. Chakraborty, K.K. Ghosh, "Geochemistry of some banded iron-formations of the Archean supracrustals, Jharkhand-Odisha region, India", Journal of Earth System Science, 116(3), pp. 245-259, 2007.
[23] A. Savitzky, M.J.E. Golay, "Soothing and differentiation of data by simplified least squares procedures", Anal. Chem., 36, pp. 1627–1639, 1964.
[24] J.M. Sunshine, C.M. Pieters, S.F. Pratt, "De-convolution of mineral absorption bands-An improved approach", Journal of Geophysical Research, 95, pp. 6955-6966, 1990.
[25] R.F. Kokaly, "Investigating a physical basis for spectroscopic estimates of leaf nitrogen concentration", Remote Sensing of Environment, 75, pp. 153– 161, 2001.
[26] Z. Malenovsky, C. Ufer, Z. Lhotáková, J.G. Clevers, M.E. Schaepman, J. Albrechtová, P. Cudlín, "A new hyperspectral index for chlorophyll estimation of a forest canopy: Area under curve normalised to maximal band depth between 650-725 nm", in EARSeL eProceedings. 5(2), pp. 161-172, 2006.
[27] R.F. Kokaly, R.N. Clark, "Spectroscopic determination of leaf biochemistry using band-depth analysis of absorption features and stepwise multiple linear regression", Remote Sensing of Environment, 67(3), pp. 267-287, 1999.
[28] R.H. Yuhas, A.F.H. Goetz, "Comparison of airborne (AVIRIS) and Spaceborne (TM) imagery data for discriminating among semi-arid landscape endmembers", In Proceedings, Ninth Thematic Conference on Geologic Remote Sensing; Environmental Research Institute of Michigan, Ann Arbor. MI., pp. 503 – 511, 1993.
[29] F. van der Meer, W. Bakker, "CCSM: Cross Correlogram Spectral Matching", International Journal of Remote Sensing, 18, pp. 1197–1201, 1997.
[30] O.A. Carvalho, P.R. Meneses, "Spectral correlation mapper (SCM): an improvement on the spectral angle mapper (SAM)", In Summaries of the 9th JPL airborne earth science workshop; 2000: 9. JPL Publication.
[31] C.I. Chang, "An information theoretic-based approach to spectral variability, similarity and discriminability for hyperspectral image analysis", IEEE Trans. Inf. Theory, 46 (5), pp. 1927–1932, 2000.
[32] Indian Bureau of Mines, Indian minerals yearbook – 2012, vol II, Metals and alloys, Ministry of Mines, Govt of India, 2012.
[33] K. Loague, R. Green, "Statistical and graphical methods for evaluating solute transport models: overview and applications", Journal of Contaminant Hydrology, 7, pp. 51–73, 1991.
[34] R.V. Morris, C.A. Lawson, E.K.J. Gibson, H.V.J. Lauer, G.A. Nace, C. Stewart, "Spectral and other physicochemical properties of submicron powders of hematite (alpha-Fe_2O_3), maghemite (gamma-Fe_2O_3), magnetite (Fe_3O_4), goethite (alpha-FeOOH), and lepidocrocite (gamma-FeOOH). J. Geophys. Res. 90, pp. 3126–3144, 1985.
[35] D.M. Sherman, T.D. Waite, "Electronic spectra of Fe oxides and oxide hydroxides in the near IR to near UV", Am. Mineral. 70, pp. 1262-1269, 1985.
[36] G.R. Hunt, "Spectral signature of particulate minerals in the visible and near infrared", Geophysics, 42, pp. 501-513, 1977.
[37] G.R. Hunt, R.P. Ashley, "Spectra of altered rocks in the visible and near infrared", Economic Geology, 74(7), pp. 1613-1629, 1979.
[38] D.J. Vaughan, J.A. Tossell, "Major transition-metal oxide minerals, their electronic structures and the interpretation of mineralogical properties", The Canadian Mineralogist, 16(2), pp. 159-168, 1978.
[39] W.F. Buckingham, "A mineralogical characterization of rock surfaces formed by hydrothermal alteration and weathering--Application to remote sensing", Ph.D. dissertation, 186 pp., Univ. of Md., College Park, Oct. 1981.
[40] F.D. van der Meer, S.M. de Jong, "Imaging spectrometry, basic principles and prospective applications", Springer, Dordrecht: the Netherlands, 2006.
[41] T. Jarmer, B. Schütt, "Analysis of iron contents in carbonate bedrock by spectro-radiometric detection based on experimentally designed substrates", In 1st EARSeL Workshop on Imaging Spectroscopy, Remote Sensing Laboratories, University of Zurich, Switzerland, 375-382, 1998.
[42] B.C. Deaton, W.L. Balsam, "Visible spectroscopy – a rapid method for determining hematite and goethite concentration in geological materials", Journal of Sedimentary Petrology, 61(4), pp. 628–632, 1991.
[43] F.T. Barranco, W.L. Balsam, B.C. Deaton, "Quantitative reassessment of brick red lutites - evidence from reflectance spectrometery", Marine Geology, 89(3–4), pp. 299–314, 1989.
[44] C.S. Kosmas, N. Curi, R.B. Bryant, D.P. Franzmeier, "Characterization of iron oxide minerals by 2nd-derivative visible spectroscopy", Soil Science Society of America Journal, 48(2), pp. 401–405, 1984.
[45] A.C. Scheinost, A. Chavernas, V. Barrón, J. Torrent, J., "Use and limitations of second-derivative diffuse reflectance spectroscopy in the visible to near infrared range to identify and quantify Fe oxide minerals in soils", Clays and Clay Minerals, 46(5), pp. 528–536, 1998.
[46] F. Tsai, W. Philpot, "Derivative analysis of hyperspectral data", Remote Sensing of Environment, 66(1), pp. 41–51, 1998.

Author Profile

Sk Wasim Akram obtained M.Sc from Vidyasagar University, West Bengal and presently pursuing Ph. D at the same institution. Currently he is serving as GIS expert under Govt. of West Bengal.

Dr Dibyendu Dutta received his Ph.D degree from Indian Agricultural Research Institute, New Delhi and served Indian Space Research Organization at different capacities for 30 years. Presently he is the Executive Director, Metis & Janus Limited, European Union and consultant for Govt. of West Bengal.

Dr Jatisankar Bandyopadhyay received M.Sc degree in Applied Geology and M.Phil, Ph.D in Environmental Geology. Currently he is Director, Centre for Environmental Studies and Head, Department of Remote Sensing, Vidyasagar University, Midnapore, West Bengal.

Annexure - 1: Ground photo of some of the sampling locations

(North East of Joda East)
22.01528°N, 85.44083°E

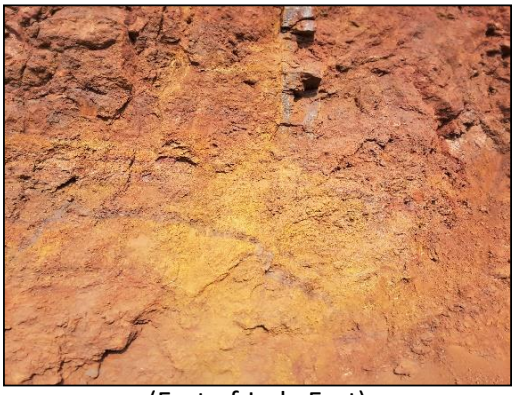

(East of Joda East)
22.01278°N, 85.43972°E

(West of Joda)
22.0214°N, 85.39633°E

(West of Hudisahi)
22.02844°N, 85.4071°E

(North west of Belkundi)
22.13187°N, 85.3939°E

(North of Murgabeda camp)
22.09805°N, 85.44995°E

(West of Koira)
21.9007°N, 85.22978°E

(East of Sreikela)
21.75472°N, 85.16278°E